Progress In Electromagnetics Research, Vol. 121, 409–431, 2011

3D BISTATIC OMEGA-K IMAGING ALGORITHM FOR NEAR RANGE MICROWAVE IMAGING SYSTEMS WITH BISTATIC PLANAR SCANNING GEOMETRY

Y. L. Qi*, W. X. Tan, Y. P. Wang, W. Hong, and Y. R. Wu

The National Key Laboratory of Microwave Imaging Technology, Institute of Electronics, Chinese Academy of Sciences, Beijing 100190, China

Abstract—By introducing bistatic geometry to near range microwave imaging systems, this paper proposes a near range three dimensional (3D) bistatic imaging geometry based on planar scanning aperture and establishes corresponding echo model. Then, the paper deduces the 3D bistatic Omega-K imaging algorithm based on implicit spectral decomposition, in which the impacts of residual phase, including position displacement, range, azimuth and elevation defocusing, are analyzed and compensated. Finally, the 3D bistatic imaging geometry and algorithm are investigated and verified via numerical simulations and experiments using a near range imaging system.

1. INTRODUCTION

Near range microwave imaging systems are considered one of the most promising systems for applications in the field of concealed weapon detection, biomedical imaging, non-destructive testing, etc. Based on the amplitude and phase information recorded by scanning a planar aperture in two orthogonal directions and transmitting broadband signals in range direction, the systems can reconstruct 3D complex image and obtain the shape, structure, and scattering properties of interested targets in the illuminated scene [1–4]. Meanwhile, near range microwave imaging technique has advantages of penetrating, security and high resolution comparing with other imaging techniques such as visible light, infrared light, X-ray, etc. [2, 5, 6].

Received 2 September 2011, Accepted 17 October 2011, Scheduled 2 November 2011
* Corresponding author: Yaolong Qi (longgniy@163.com).

Bistatic geometry is characterized by separated transmitter and receiver. And bistatic imaging system can exploit non-backscattering information included in the bistatic reflectivity of targets, which is helpful to classify and identify different kinds of targets [7, 8].

By introducing bistatic geometry to near range microwave imaging system, this paper proposes 3D bistatic imaging geometry. Specially, the bistatic range equation is a dual square root, resulting that the monostatic algorithms cannot be applied to bistatic geometry. Some two dimensional (2D) bistatic algorithms [9, 10] are modified from monostatic algorithms by means of making approximations and simplifications to the dual square root. The common shortcoming of these algorithms is their rigorous applying conditions. Based on the principle of implicit spectral decomposition, Ender [11] proposed a method which adopted a linear fit of the phase term in wavenumber domain which can minimize the residual phase error. QIU [7] deduced an Omega-K algorithm in which the impacts of remaining phase errors are studied and a compensation method is proposed. However, these algorithms which are developed particularly for bistatic geometry [7, 12–14] are mostly deduced for 2D case, and only the 2D complex image of scene can be reconstructed. This paper deduces the 3D bistatic Omega-K imaging algorithm for near range microwave imaging systems and analyzes the impacts of residual phase.

The structure of the paper is organized as follows. 3D bistatic imaging geometry based on planar scanning aperture and corresponding echo model are established in Section 2. Then, in Section 3, the paper deduces the 3D bistatic Omega-K algorithm based on implicit spectral decomposition, and analyzes the impacts of residual phase, including position displacement, range, azimuth and elevation defocusing. Finally, the correctness of the imaging geometry and imaging algorithm are verified via numerical simulations and near range imaging experiment in Section 4. Section 5 provides several conclusions.

2. 3D BISTATIC IMAGING GEOMETRY

In this section, 3D bistatic imaging geometry and corresponding echo model are established and analyzed. Firstly, Subsection 2.1 analyzes the 3D bistatic imaging geometry [2, 16, 15–18], which is formed by scanning a planar aperture in two orthogonal directions and transmitting broadband signals in range direction. Then, based on the geometry, Subsection 2.2 establishes the corresponding echo model.

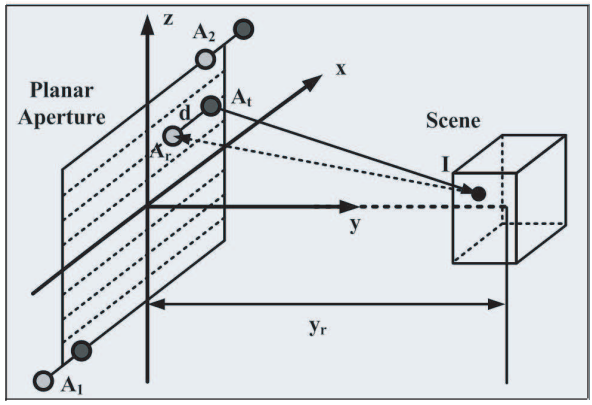

Figure 1. 3D bistatic imaging geometry.

2.1. Imaging Geometry

As shown in Fig. 1, by setting the center of scanning plane to be the origin of the Cartesian coordinates, the directions of range, azimuth and elevation are denoted as Y, X and Z axes, respectively.

The transceiver consists of transmitter A_t and receiver A_r, with azimuth interval of d. As shown in Fig. 1, the transceiver moves along azimuth and elevation directions to synthesize planar scanning aperture on the plane $x-z$, with initial scanning position A_1 and final scanning position A_2. Denote the instantaneous scanning position as $A(x', 0, z')$, then the coordinates of transmitting and receiving antennas can be expressed as $A_t(x' + \frac{d}{2}, 0, z')$ and $A_r(x' - \frac{d}{2}, 0, z')$.

Besides, y_r is the distance of scene center from the aperture, and I indicates an arbitrary point scatterer located at (x, y, z).

2.2. Echo Model

Suppose that the 3D complex reflectivity function of the distributed targets in Cartesian coordinates is $I(x, y, z)$. In this case, the measured echoes [1, 2] from a given point scatterer located at $(x,\ y,\ z)$ can be written as,

$$E_I\left(x', K_\omega, z'\right) = I\left(x, y, z\right) \exp\left(-jK_\omega R_{bi}\right) \tag{1}$$

where K_ω is frequency wavenumber of stepped frequency continuous wave signal, and is related to instantaneous frequency f, the speed of light c via $K_\omega = \frac{2\pi f}{c}$. $K_\omega \in [K_{\omega\,\min}, K_{\omega\,\max}]$, where $K_{\omega\,\min}$ and $K_{\omega\,\max}$ are the wavenumbers at minimum and maximum frequencies, respectively. And R_{bi} is the two-way distance between the transceiver

in scanning position $A(x', 0, z')$ and an arbitrary point scatterer located at (x, y, z),

$$R_{bi} = R_t + R_r = \sqrt{\left(x' + \frac{d}{2} - x\right)^2 + y^2 + (z' - z)^2} + \sqrt{\left(x' - \frac{d}{2} - x\right)^2 + y^2 + (z' - z)^2} \quad (2)$$

Therefore, the response measured at scanning position $A(x', 0, z')$ has the following form,

$$E_{R_{bi}}\left(x', K_\omega, z'\right) = \iiint_{\mathbf{V}} E_I\left(x', K_\omega, z'\right) d\mathbf{r} = \iiint_{\mathbf{V}} I\left(x, y, z\right) \exp\left(-jK_\omega R_{bi}\right) d\mathbf{r} \quad (3)$$

where $\mathbf{V}$ denotes the illuminated area, $\mathbf{r}$ is position vector of the targets and $d\mathbf{r} = dxdydz$. $|x' - x| \leq \frac{L_x}{2}$ and $|z' - z| \leq \frac{L_z}{2}$, where L_x and L_z are the synthetic aperture lengths of azimuth and elevation, which are determined by -3 dB beam width ϕ_x in azimuth and ϕ_z in elevation.

3. 3D OMEGA-K ALGORITHM FOR 3D BISTATIC IMAGING GEOMETRY

This section deduces the 3D bistatic Omega-K imaging algorithm based on implicit spectral decomposition, in which the residual phase is analyzed and compensated.

3.1. Echo Spectrum in Wavenumber Domain

By performing two dimensional FFT with respect to x' and z', and interchanging the order of the integrals, the echoes in (3) can be rewritten as,

$$E_{R_{bi}}\left(K_x, K_\omega, K_z\right) = \iiint_{\mathbf{V}} I\left(x, y, z\right) \times \left\{\int_{x'}\int_{z'} \exp\left(-jK_\omega R_{bi} - jK_x x' - jK_z z'\right) dx'dz'\right\} d\mathbf{r} \quad (4)$$

Let $u = x' - x$, $v = z' - z$, and (4) becomes,

$$E_{R_{bi}}(K_x, K_\omega, K_z) = \iiint_{\mathbf{V}} I\left(x, y, z\right) \exp\left(-jK_x x - jK_z z\right) \times \left\{\int_u\int_v \exp[-j\left(K_\omega R_{bi} + K_x u + K_z v\right)] dudv\right\} d\mathbf{r} \quad (5)$$

Denote $\Phi(u,v)$ as the phase of the last integral term in (5),

$$\Phi(u,v) = K_\omega R_{bi}(u,v) + K_x u + K_z v \tag{6}$$

where

$$R_{bi}(u,v) = \sqrt{\left(u+\frac{d}{2}\right)^2 + y^2 + v^2} + \sqrt{\left(u-\frac{d}{2}\right)^2 + y^2 + v^2} \tag{7}$$

According to the method of stationary phase (MSP), it is necessary to solve the stationary point $(u^*,\ v^*)$ for computing the spectrum in (5), and $(u^*,\ v^*)$ should satisfy,

$$\frac{\partial\Phi}{\partial u}|_{(u^*,v^*)} = 0, \qquad \frac{\partial\Phi}{\partial v}|_{(u^*,v^*)} = 0 \tag{8}$$

i.e.,

$$\begin{aligned} \frac{u^*+\frac{d}{2}}{\sqrt{\left(u^*+\frac{d}{2}\right)^2 + y^2 + v^{*2}}} + \frac{v^*-\frac{d}{2}}{\sqrt{\left(u^*-\frac{d}{2}\right)^2 + y^2 + v^{*2}}} &= -\frac{K_x}{K_\omega} \\ \frac{v^*}{\sqrt{\left(u^*+\frac{d}{2}\right)^2 + y^2 + v^{*2}}} + \frac{v^*}{\sqrt{\left(u^*-\frac{d}{2}\right)^2 + y^2 + v^{*2}}} &= -\frac{K_z}{K_\omega} \end{aligned} \tag{9}$$

Let $C_1 = K_x/K_\omega$, $C_2 = K_z/K_\omega$, then u^* and v^* are functions of C_1, C_2 and y, which are denoted as $u^* = u^*(C_1, C_2, y)$ and $v^* = v^*(C_1, C_2, y)$. Then, the stationary phase can be expressed as,

$$\begin{aligned} \Phi(u^*,v^*) &= K_\omega\left[R_{bi}(C_1,C_2,y) + C_1 u^*(C_1,C_2,y) + C_2 v^*(C_1,C_2,y)\right] \\ &= K_\omega\Bigg\{\sqrt{\left[u^*(C_1,C_2,y)+\frac{d}{2}\right]^2 + y^2 + v^*(C_1,C_2,y)^2} \\ &\quad + \sqrt{\left[u^*(C_1,C_2,y)-\frac{d}{2}\right]^2 + y^2 + v^*(C_1,C_2,y)^2} \\ &\quad + C_1 u^*(C_1,C_2,y) + C_2 v^*(C_1,C_2,y)\Bigg\} \end{aligned} \tag{10}$$

Then, the implicit spectrum in wavenumber domain of the echo in (5) can be written as,

$$\begin{aligned} E_{R_{bi}}(K_x,K_\omega,K_z) = \iiint_{\mathbf{V}} & I(x,y,z)\exp(-jK_x x - jK_z z) \\ & \{\exp[-j\Phi(u^*,v^*)]\}\,d\mathbf{r} \end{aligned} \tag{11}$$

If the last exponential term in (11) is separable [11], that is,

$$\begin{aligned} \Phi(u^*,v^*) &= K_\omega\left[R_{bi}(C_1,C_2,y) + C_1 u^*(C_1,C_2,y) + C_2 v^*(C_1,C_2,y)\right] \\ &= K_\omega\left[h(C_1,C_2)\,q(y) + g(C_1,C_2)\right] \end{aligned} \tag{12}$$

then, the 3D complex image of the scene can be reconstructed through compensating the phase $K_\omega g(C_1, C_2)$ which is independent of y, performing a wavenumber domain interpolation which can transform the data from (K_x, K_ω, K_z) domain to $[K_x, K_\omega h(C_1, C_2), K_z]$ domain, and finally performing a 3D IFFT [2, 7].

However, different from monostatic 3D imaging geometry, the bistatic range equation is a dual square root, resulting that the term is not separable, and only an approximate solution can be found.

3.2. Interpolation in wavenumber domain

This subsection achieves the factorization of $\Phi(u^*, v^*)$ in (12). Denote the scene center as reference position y_r and expand $\Phi(u^*, v^*)$ to its Taylor series at y_r, that is,

$$\begin{aligned}\Phi\left(u^*, v^*\right) &= \Phi\left(C_1, C_2; y_r\right) + \frac{\partial \Phi}{\partial y}\Big|_{y_r}\left(y - y_r\right) + \frac{1}{2!}\frac{\partial^2 \Phi}{\partial y^2}\Big|_{y_r}\left(y - y_r\right)^2 \\ &\quad + \frac{1}{3!}\frac{\partial^3 \Phi}{\partial y^3}\Big|_{y_r}\left(y - y_r\right)^3 + O\left[\left(y - y_r\right)^4\right] \end{aligned} \tag{13}$$

where

$$\begin{aligned}\frac{\partial \Phi}{\partial y}\Big|_{y_r} &= K_\omega \Bigg\{ \frac{y_r}{\sqrt{\left[u^*\left(C_1, C_2, y_r\right) + \frac{d}{2}\right]^2 + y_r^2 + \left[v^*\left(C_1, C_2, y_r\right)\right]^2}} \\ &\quad + \frac{y_r}{\sqrt{\left[u^*\left(C_1, C_2, y_r\right) - \frac{d}{2}\right]^2 + y_r^2 + \left[v^*\left(C_1, C_2, y_r\right)\right]^2}} \Bigg\} \\ &\quad + K_\omega \left(\frac{\partial \Phi}{\partial u}\Big|_{(u^*, v^*)} \frac{\partial u}{\partial y}\Big|_{y_r} \right) + K_\omega \left(\frac{\partial \Phi}{\partial v}\Big|_{(u^*, v^*)} \frac{\partial v}{\partial y}\Big|_{y_r} \right) \end{aligned} \tag{14}$$

According to (8), the second and third terms in (14) are zero, therefore, (14) can be simplified to be,

$$\begin{aligned}\frac{\partial \Phi}{\partial y}\Big|_{y_r} &= K_\omega \Bigg\{ \frac{y_r}{\sqrt{\left[u^*\left(C_1, C_2, y_r\right) + \frac{d}{2}\right]^2 + y_r^2 + \left[v^*\left(C_1, C_2, y_r\right)\right]^2}} \\ &\quad + \frac{y_r}{\sqrt{\left[u^*\left(C_1, C_2, y_r\right) - \frac{d}{2}\right]^2 + y_r^2 + \left[v^*\left(C_1, C_2, y_r\right)\right]^2}} \Bigg\} \end{aligned} \tag{15}$$

Let

$$K_y = K_\omega \cdot h\left(C_1, C_2\right) = K_\omega \cdot \frac{\partial \Phi}{\partial y}\Big|_{y_r} \tag{16}$$

then, after compensating the phase $\Phi(C_1, C_2; y_r)$ which is irrelevant to y, the data can be transformed from (K_x, K_ω, K_z) domain to (K_x, K_y, K_z) domain via interpolation according to (16).

3.3. Residual Phase Compensation

After wavenumber domain interpolation according to (16), the residual item in (13) is called residual phase, which is analyzed in this subsection [7].

In (13), define,

$$p\left(K_x, K_\omega, K_z\right) = \frac{\partial^2 \Phi}{\partial y^2}\Big|_{y_r}, f\left(K_x, K_\omega, K_z\right) = \frac{\partial^3 \Phi}{\partial y^3}\Big|_{y_r} \tag{17}$$

Then, the residual phase in (13) becomes,

$$\begin{aligned}\Phi_{res}\left(K_x, K_y, K_z; y\right) &= K_y\left(y - y_r\right) + \frac{1}{2!}p\left(K_x, K_y, K_z\right)\left(y - y_r\right)^2 \\ &\quad + \frac{1}{3!}f\left(K_x, K_y, K_z\right)\left(y - y_r\right)^3 \end{aligned} \tag{18}$$

Define that K_{x0}, K_{y0} and K_{z0} are the central values of K_x, K_y and K_z, respectively. Then, by expanding $p(K_x, K_y, K_z)$ and $f(K_x, K_y, K_z)$ to their Taylor series at K_{y0} and retaining the first three terms, the residual phase can be expressed as,

$$\begin{aligned}\Phi_{res}\left(K_x, K_y, K_z; y\right) &= K_{y0}\left(y - y_r\right) + \left(K_y - K_{y0}\right) q\left(K_x, K_z; y\right) \\ &\quad + \Phi_{err}^{rg}\left(K_x, K_y, K_z; y\right) + \Phi_{res}^{pl}\left(K_x, K_{y0}, K_z; y\right)\end{aligned} \tag{19}$$

where

$$\begin{aligned}q\left(K_x, K_z; y\right) &= \left(y - y_r\right) + \frac{1}{2!}\frac{\partial p\left(K_x, K_y, K_z\right)}{\partial K_y}\Big|_{K_{y0}}\left(y - y_r\right)^2 \\ &\quad + \frac{1}{3!}\frac{\partial f\left(K_x, K_y, K_z\right)}{\partial K_y}\Big|_{K_{y0}}\left(y - y_r\right)^3 \end{aligned} \tag{20}$$

$$\begin{aligned}\Phi_{err}^{rg}\left(K_x, K_y, K_z; y\right) &= \left(K_y - K_{y0}\right)^2 \\ &\quad \times \left[\frac{1}{2!}\frac{\partial^2 p\left(K_x, K_y, K_z\right)}{\partial K_y^2}\Big|_{K_{y0}}\left(y - y_r\right)^2\right. \\ &\quad \left. + \frac{1}{3!}\frac{\partial^2 f\left(K_x, K_y, K_z\right)}{\partial K_y^2}\Big|_{K_{y0}}\left(y - y_r\right)^3\right] \end{aligned} \tag{21}$$

$$\begin{aligned}\Phi_{res}^{pl}\left(K_x, K_{y0}, K_z; y\right) &= \frac{1}{2!}p\left(K_x, K_{y0}, K_z\right)\left(y - y_r\right)^2 \\ &\quad + \frac{1}{3!}f\left(K_x, K_{y0}, K_z\right)\left(y - y_r\right)^3 \end{aligned} \tag{22}$$

In (21), (22), Φ_{err}^{rg} is range phase error, Φ_{res}^{pl} is the residual phase term which is relevant to azimuth and elevation variables.

Again, by expanding $p(K_x, K_{y0}, K_z)$ and $f(K_x, K_{y0}, K_z)$ to their Taylor series at (K_{x0}, K_{z0}) and retaining the first three terms, (22) becomes,

$$\begin{aligned}\Phi_{res}^{pl}(K_x, K_{y0}, K_z; y) = {} & x_m(y) + z_m(y) \\ & + \Phi_{err}^{az}(K_x; y) + \Phi_{err}^{el}(K_z; y) + \Phi_{err}^{ae}(K_x; K_z; y) \\ & + \frac{1}{2!} p(K_{x0}, K_{y0}, K_{z0})(y - y_r)^2 \\ & + \frac{1}{3!} f(K_{x0}, K_{y0}, K_{z0})(y - y_r)^3 \end{aligned} \tag{23}$$

where

$$\begin{aligned} x_m(y) = {} & (K_x - K_{x0}) \left[\frac{1}{2!} \frac{\partial p(K_x, K_{y0}, K_z)}{\partial K_x}\Big|_{(K_{x0}, K_{z0})} (y - y_r)^2 \right. \\ & \left. + \frac{1}{3!} \frac{\partial f(K_x, K_{y0}, K_z)}{\partial K_x}\Big|_{(K_{x0}, K_{z0})} (y - y_r)^3 \right] \end{aligned} \tag{24}$$

$$\begin{aligned} z_m(y) = {} & (K_z - K_{z0}) \left[\frac{1}{2!} \frac{\partial p(K_x, K_{y0}, K_z)}{\partial K_z}\Big|_{(K_{x0}, K_{z0})} (y - y_r)^2 \right. \\ & \left. + \frac{1}{3!} \frac{\partial f(K_x, K_{y0}, K_z)}{\partial K_z}\Big|_{(K_{x0}, K_{z0})} (y - y_r)^3 \right] \end{aligned} \tag{25}$$

$$\begin{aligned} \Phi_{err}^{az}(K_x; y) = {} & \frac{1}{2!}(K_x - K_{x0})^2 \left[\frac{1}{2!} \frac{\partial^2 p(K_x, K_{y0}, K_z)}{\partial K_x^2}\Big|_{(K_{x0}, K_{z0})} (y - y_r)^2 \right. \\ & \left. + \frac{1}{3!} \frac{\partial^2 f(K_x, K_{y0}, K_z)}{\partial K_x^2}\Big|_{(K_{x0}, K_{z0})} (y - y_r)^3 \right] \end{aligned} \tag{26}$$

$$\begin{aligned} \Phi_{err}^{el}(K_z; y) = {} & \frac{1}{2!}(K_z - K_{z0})^2 \left[\frac{1}{2!} \frac{\partial^2 p(K_x, K_{y0}, K_z)}{\partial K_z^2}\Big|_{(K_{x0}, K_{z0})} \right. \\ & \left. (y - y_r)^2 + \frac{1}{3!} \frac{\partial^2 f(K_x, K_{y0}, K_z)}{\partial K_z^2}\Big|_{(K_{x0}, K_{z0})} (y - y_r)^3 \right] \end{aligned} \tag{27}$$

$$\begin{aligned} \Phi_{err}^{ae}(K_x, K_z; y) = {} & (K_x - K_{x0})(K_z - K_{z0}) \\ & \times \left[\frac{1}{2!} \frac{\partial^2 p(K_x, K_{y0}, K_z)}{\partial K_x \partial K_z}\Big|_{(K_{x0}, K_{z0})} (y - y_r)^2 \right. \\ & \left. + \frac{1}{3!} \frac{\partial^2 f(K_x, K_{y0}, K_z)}{\partial K_x \partial K_z}\Big|_{(K_{x0}, K_{z0})} (y - y_r)^3 \right] \end{aligned} \tag{28}$$

According to (19)–(28), the residual phase in (18) is,

$$\begin{aligned}\Phi_{res}(K_x, K_y, K_z; y) \;=\; & \Phi_{const} + (K_y - K_{y0})\, q(K_x, K_z; y) + x_m(y) \\ & + z_m(y) + \Phi_{err}^{rg}(K_x, K_y, K_z; y) + \Phi_{err}^{az}(K_x; y) \\ & + \Phi_{err}^{el}(K_z; y) + \Phi_{err}^{ae}(K_x, K_z; y) \end{aligned} \tag{29}$$

Then, after removing the phase $\Phi(C_1, C_2; y_r)$ and performing wavenumber domain interpolation, the echo spectrum in (11) becomes,

$$\begin{aligned} E_{R_{bi}}(K_x, K_y, K_z) = & \iiint_{\mathbf{V}} I(x, y, z) \exp(-jK_x x - jK_z z) \\ & \times \exp\Big\{-j\Big[\Phi_{const} + (K_y - K_{y0})\, q(K_x, K_z; y) + x_m(y) \\ & + z_m(y) + \Phi_{err}^{rg} + \Phi_{err}^{az} + \Phi_{err}^{el} + \Phi_{err}^{ae}\Big]\Big\} d\mathbf{r} \end{aligned} \tag{30}$$

Based on (29) and (30), the impacts of each term are analyzed as follows, meanwhile, the procedures of residual phase compensation are discussed.

1) Const phase: The const phase Φ_{const} has no impact on the focusing quality.

$$\begin{aligned} \Phi_{const} = & K_{y0}(y - y_r) + \frac{1}{2!} p(K_{x0}, K_{y0}, K_{z0})(y - y_r)^2 \\ & + \frac{1}{3!} f(K_{x0}, K_{y0}, K_{z0})(y - y_r)^3 \end{aligned} \tag{31}$$

2) Position displacement: The linear phase terms in (29) and (30) will result in the position displacements.

Range position: Performing an IFFT with respect to K_y, the targets located at range y will appear at $q(K_x, K_z; y)$ in $(K_x, K_z; q)$ domain. Therefore, the algorithm will finally give an image in (x, q, z) domain, where q depends on (K_x, K_z). And the range y should meet the following inequality in order to ensure all the targets in the scene can be well focused [7],

$$\max[q(K_x, K_z; y)] - \min[q(K_x, K_z; y)] \le \Delta q \tag{32}$$

where Δq indicates the range interval of the image. And the targets located at range y will appear at $q(K_{x0}, K_{z0}; y)$ when (32) is satisfied.

After IFFT with respect to K_y, (30) becomes,

$$\begin{aligned} E_{R_{bi}}(K_x, q, K_z) = & \int_x \int_z I(x, q, z) \exp(-jK_x x - jK_z z)\, dx dz \\ & \times \exp\Big\{-j\Big[x_m(y) + z_m(y) + \Phi_{err}^{rg} + \Phi_{err}^{az} + \Phi_{err}^{el} + \Phi_{err}^{ae}\Big]\Big\} \end{aligned} \tag{33}$$

Azimuth and Elevation position: According to (11), (23)–(25), (33), if performing IFFT with respect to K_x and K_z, the targets located at x, z will appear at $x + x_m(y)$, $z + z_m(y)$. It can be seen that $x_m(y_r) = z_m(y_r) = 0$ and $x_m(y)$, $z_m(y)$ increase with $|y - y_r|$. Therefore, the targets at reference range y_r will appear in the correct positions, while targets beyond y_r will deviate from their original positions.

3) Range phase error: $\Phi_{err}^{rg}(K_x, K_y, K_z; y)$ is range phase error, which is usually very small (less than 0.05 rad in the simulation of this paper) and can be ignored.

4) Azimuth and elevation phase error: $\Phi_{err}^{az}(K_x; y)$ and $\Phi_{err}^{el}(K_z; y)$, that is, the azimuth and elevation phase error will degrade the focusing quality of azimuth and elevation. According to (26) and (27), $\Phi_{err}^{az}(K_x; y_r) = 0$, $\Phi_{err}^{el}(K_z; y_r) = 0$ and both of the two terms increase with $|y - y_r|$. Therefore, the targets at reference range y_r will not be affected, while targets at boundary of the scene will suffer the greatest impact. Similarly, the phase error $\Phi_{err}^{ae}(K_x; K_z; y_r)$ which is related to both of azimuth and elevation and called cross phase error in this paper, has no effect on targets at reference range, while affecting the boundary targets.

5) Residual Phase Compensation: Based on the analysis in *2)–4)*, the paper compensates the residual phase with the filter H_{comp} in (K_x, y, K_z) domain (i.e., (K_x, q, K_z) domain),

$$\begin{aligned} H_{comp}(K_x, K_z; y) \;=\; & \exp\left\{ j[x_m(y) + z_m(y) + \Phi_{err}^{az}(K_x; y) \right. \\ & \left. + \Phi_{err}^{el}(K_z; y) + \Phi_{err}^{ae}(K_x; K_z; y)] \right\} \end{aligned} \tag{34}$$

Denote the signal after compensation as E_{Comp}, then, (33) becomes,

$$E_{Comp}(K_x, q, K_z) = \int_x \int_z I(x, q, z) \exp(-jK_x x - jK_z z)\, dxdz \tag{35}$$

from which the 3D complex image in (x, q, z) domain can be reconstructed by performing 2D IFFT with respect to K_x and K_z.

3.4. Reconstruction procedure

Based on the analysis of Subsection 3.2–3.3, the block diagram [2, 7, 15, 16] of 3D bistatic Omega-K algorithm, which is based on implicit spectral decomposition and includes the procedure of residual phase compensation, can be summarized as shown in Fig. 2.

Step 1. Performing 2D FFT with respect to x' and z'.

Step 2. Compensating the phase $\Phi(C_1, C_2; y_r)$ which is irrelevant to y.

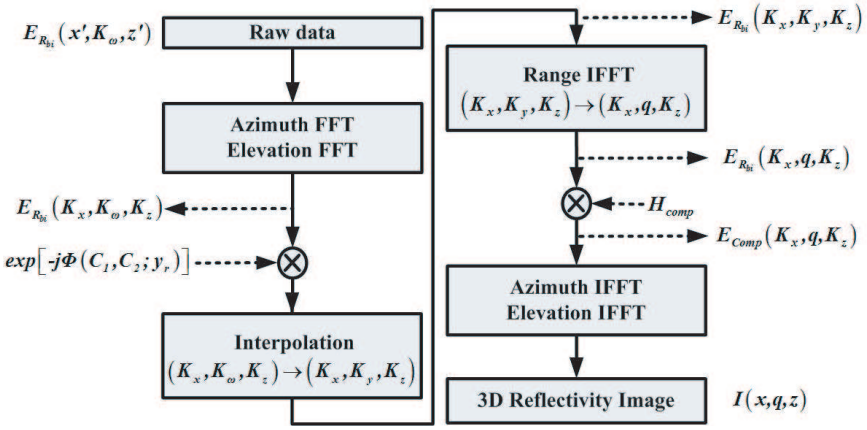

Figure 2. Block diagram of 3D bistatic Omega-K algorithm.

Step 3. Performing wavenumber domain interpolation to transform the data from (K_x, K_ω, K_z) domain to (K_x, K_y, K_z) domain.

Step 4. Performing IFFT with respect to K_y.

Step 5. Compensating the residual phase.

Step 6. Performing 2D IFFT with respect to K_x and K_z.

Some implementation details are described as follows.

1) Wavenumber domain interpolation in Step 3. Wavenumber domain interpolation can be achieved through the following sub-steps.

Calculation of $u^*(C_1, C_2, y)$ and $v^*(C_1, C_2, y)$. For each K_x, K_ω and K_z, the stationary point $u^*(C_1, C_2, y)$ and $v^*(C_1, C_2, y)$ can be found by means of numerical calculation through (9).

Calculation of K_y. Based on the result of $u^*(C_1, C_2, y)$ and $v^*(C_1, C_2, y)$, K_y can be solved through (16). And K_y is a function of K_x, K_ω and K_z. Then, wavenumber domain interpolation can be achieved.

2) Residual phase compensation in Step 5. The calculation of H_{comp} mainly includes the following sub-steps.

Calculation of $\Phi(u^*, v^*)$. For some fixed K_x^i, K_y^j and K_z^k, where $i = 1, 2, ..., l$, $j = 1, 2, ..., m$ and $k = 1, 2, ..., n$. And l, m and n are the numbers of control points, respectively. $K_\omega^{i,j,k}$ corresponding to K_x^i, K_y^j and K_z^k can be calculated using numerical methods through (16). Then $\Phi[u^*(K_x^i, K_\omega^{i,j}, y), v^*(K_z^k, K_\omega^{k,j}, y)]$ versus y can be solved.

Calculation of $p(K_x, K_y, K_z)$ and $f(K_x, K_y, K_z)$. According to $\Phi(u^*, v^*)$, $p(K_x^i, K_\omega^{i,j,k}, K_z^k)$ and $f(K_x^i, K_\omega^{i,j,k}, K_z^k)$ [i.e., $p(K_x^i, K_y^j, K_z^k)$ and $f(K_x^i, K_y^j, K_z^k)$] can be solved by means of polynomial fitting

method. Then, $p(K_{x0}, K_{y0}, K_{z0})$ and $f(K_{x0}, K_{y0}, K_{z0})$ can be calculated through polynomial interpolation. Accordingly, the partial derivatives with respect to K_x, K_y and K_z can be derived by means of polynomial fitting method.

Calculation of H_{comp}. According to the partial derivatives solved above, each term of the phase error can be calculated, which can form the compensation phase of H_{comp}.

3.5. Resolution

The resolutions of the 3D complex image depend on the frequency bandwidth, center frequency and the dimensions of the synthetic aperture [2]. And the range resolution δy, azimuth resolution δx and elevation resolution δz can be expressed as,

$$\delta_x = \frac{\lambda_0 R}{2L_x}, \quad \delta_y = \frac{c}{2B}, \quad \delta_z = \frac{\lambda_0 R}{2L_z} \quad L_{x,z} = \min\left\{L'_{x,z}, \phi_{x,z} \times R\right\} \quad (36)$$

where λ_0 is the wavelength of the center frequency, B is the bandwidth, $L_{x,z}$ are the synthetic aperture lengths of azimuth and elevation, $L'_{x,z}$ are the scanning lengths of azimuth and elevation, $\phi_{x,z} = K_b\lambda_0/D_{x,z}$ are the beam width of the two directions, $K_b = 0.89$ is beam width factor, $D_{x,z}$ are the antenna physical size of azimuth and elevation, and R is distance from targets to scanning plane.

4. SIMULATIONS AND EXPERIMENTS

By means of numerical simulations and experiments based on near range imaging system, this section verifies the correctness and effectiveness of the imaging geometry and corresponding imaging algorithm of this paper.

4.1. Numerical simulations

The main simulation parameters, which are consistent with the actual parameters of near range imaging system, are listed in Table 1.

The simulation scenario is shown in Fig. 3. There are 75 point scatterers in the 3D space, divided into three groups of 25. And the range from the three groups of scatterers to scanning plane are 1.2 m, 1.5 m and 1.8 m, respectively. Besides, for the scatter targets in each group, both of the azimuth and elevation interval among adjacent targets are 0.1 m.

Theoretical resolutions can be calculated according to (36) and the simulation parameters. The range resolution is 0.025 m. The azimuth

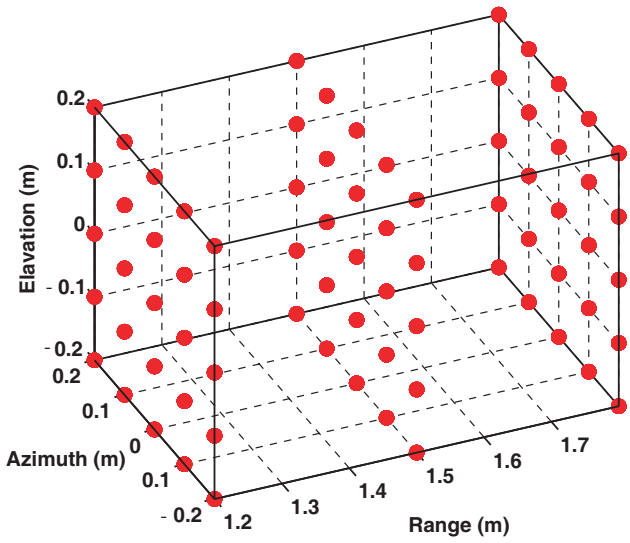

Figure 3. Simulation scene which consists of 75 point scatterers divided into three groups, and each group includes 25 ones, spaced 0.1 m in azimuth and elevation.

Table 1. Simulation parameters.

	Parameters	Value
Range	Frequency range	31–37 GHz
	Bandwidth	6 GHz
	Wavelength of center frequency	0.0088 m
	Number of frequency points	101
Azimuth/Elevation	Interval of antennas	0.5 m/0 m
	Antenna physical size	0.015 m/0.012 m
	Scanning interval	5 mm/5 mm
	Scanning length	0.65 m/0.65 m

and elevation resolutions are determined by the synthetic aperture lengths which are the smaller one of $L'_{x,z}$ and $\phi_{x,z}$ R, and the calculating procedures of azimuth and elevation resolutions are listed in Table 2.

4.1.1. Imaging Results.

In order to analyze the impacts of residual phase, both of the images based on algorithms without and with residual phase compensation are derived, and the 3D imaging results are shown in Fig. 4. The red one

Table 2. Theoretical resolutions of targets located at the range of 1.2 m, 1.5 m and 1.8 m.

	$\text{Ł}'_{x,z}$	$\phi_x\mathbf{R}$	**Azimuth**	$\phi_z\mathbf{R}$	**Elevation**
Near (1.2 m)	0.65 m	0.6282 m	0.0084 m	0.7853 m	0.0081 m
Center (1.5 m)	0.65 m	0.7853 m	0.0102 m	0.9816 m	0.0102 m
Far (1.8 m)	0.65 m	0.9423 m	0.0122 m	1.1779 m	0.0122 m

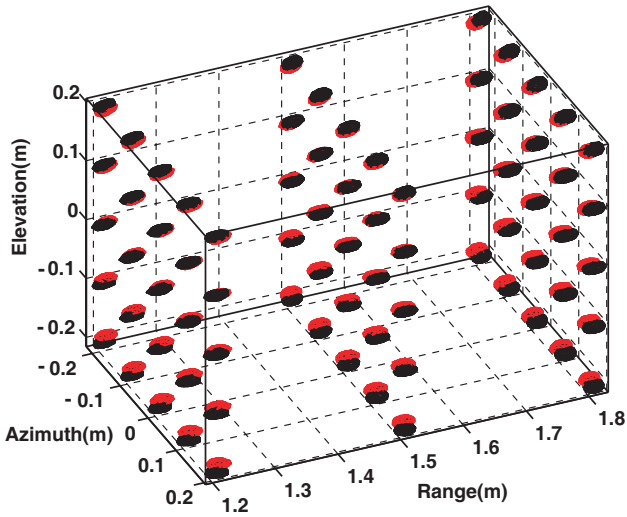

Figure 4. 3D imaging result of simulation scenario with displayed dynamic range of 13 dB.

is image without the compensation, while the black one is the image with the compensation.

4.1.2. Targets Position.

Range position. According to the analysis in Subsection 3.3, the targets located at range y will appear at $q(K_{x0}, K_{y0}; y)$ under the condition of (32), where

$$q(K_{x0}, K_{z0}; y) = y + 2.414 \times 10^{-4}(y - y_r)^2 - 5.980 \times 10^{-6}(y - y_r)^3 \quad (37)$$

Azimuth and elevation positions. Denoting the scene center as reference range y_r, then the targets at reference range will appear

in the correct azimuth and elevation positions, while targets at the boundary of scene will have largest offset from their original positions.

In order to highlight the position displacement, the displayed dynamic range of Fig. 4 is 13 dB, which means that only the main lobe of the targets are shown. It can be seen from Fig. 4 that there are certain azimuth and elevation position offset between the red and black image. The quantitative analysis can be achieved using profile method.

For analyzing the azimuth and elevation position displacement, profiles of different ranges are analyzed. It can be seen from Fig. 4 that there are three groups of targets which are in different ranges. The center targets of each group are chosen to be analyzed and their profiles are shown in Fig. 5. In the figure, (a)–(c) are results without residual phase compensation and (d)–(f) are results with compensation.

In Figs. 5(a)–(c), the azimuth displacements of near, center and far targets are 3 mm, 0 mm and 5 mm, respectively. And elevation displacements are 4 mm, 0 mm and 4 mm, respectively. However, the targets in Figs. 5(d)–(f) can be focused on right positions.

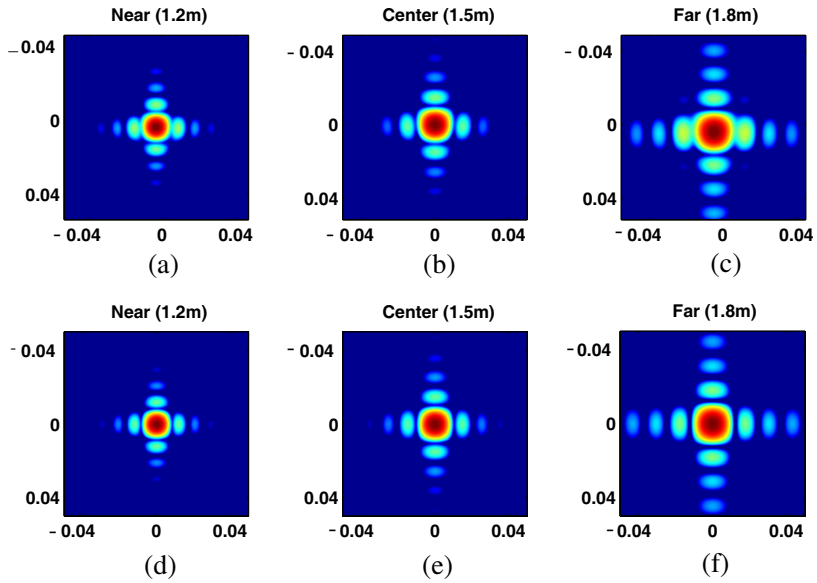

Figure 5. Contrast of the profiles without and with residual phase compensation. Horizontal axis indicates azimuth direction in units of meter, vertical axis indicates elevation direction in units of meter, and the displayed dynamic range is 25 dB. (a)–(c) are the profiles without the compensation, (d)–(f) are profiles with the compensation.

4.1.3. Focusing Quality.

The phase error can be calculated according to Subsection 3.5. The results are shown in Fig. 6. In the calculation, l, m and n are 16.

Range phase error. $\Phi_{err}^{rg}(K_x, K_{yb}, K_z; y)$ in (21) is the range phase error, where K_{yb} is the border of K_y. However, $\Phi_{err}^{rg}(K_x, K_{yb}, K_z; y)$ is a triple function which is inconvenient to display. Therefore, K_z might be fixed in the border K_{zb} and the result of $\Phi_{err}^{rg}(K_x, K_{yb}, K_{zb}; y)$ is shown in Fig. 6(a). It can be seen that the range phase error is less than 0.05 rad which has little effect on focusing quality of range.

Azimuth and elevation phase error. The results of Φ_{err}^{az}, Φ_{err}^{el} and Φ_{err}^{ae} in (26)–(28) are shown in Figs. 6(b)–(d), respectively. Similarly, $\Phi_{err}^{az}(K_x, K_{yb}, K_{zb}; y)$, $\Phi_{err}^{el}(K_{xb}, K_{yb}, K_z; y)$ and $\Phi_{err}^{ae}(K_x, K_{yb}, K_{zb}; y)$ are shown for the convenience of display. It can be seen that the phase error terms are zero in reference range, while have largest value in boundary of range direction. Besides, the azimuth phase error is much larger than elevation phase error.

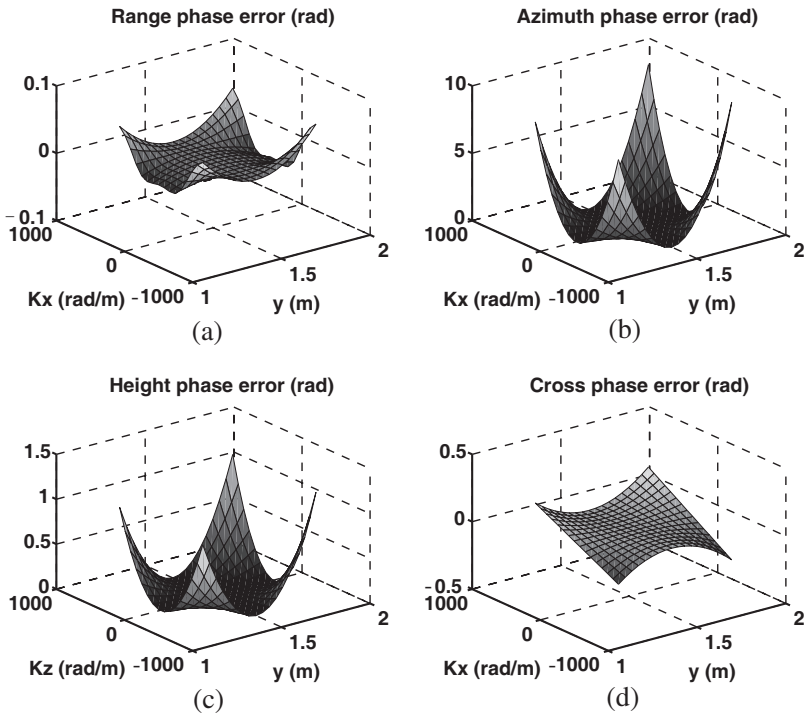

Figure 6. Phase error which will degrade the focusing quality.

Table 3. Focusing quality of scatterers in different ranges. The azimuth and elevation IRW and PSLR of the imaging result with residual phase compensation are improved comparing with the result without the compensation.

Location		**Without Compensation**		**With Compensation**	
		IRW	PSLR	IRW	PSLR
Near 1.2 m	Range	0.02531 m	−13.10 dB	0.02521 m	−13.36 dB
	Azimuth	0.00856 m	−11.72 dB	0.00842 m	−13.41 dB
	Elevation	0.00821 m	−12.88 dB	0.00816 m	−13.27 dB
Center 1.5 m	Range	0.02512 m	−13.30 dB	0.02510 m	−13.30 dB
	Azimuth	0.01022 m	−13.29 dB	0.01021 m	−13.31 dB
	Elevation	0.01023 m	−13.33 dB	0.01023 m	−13.34 dB
Far 1.8 m	Range	0.02531 m	−13.26 dB	0.02524 m	−13.35 dB
	Azimuth	0.01239 m	−11.75 dB	0.01223 m	−13.44 dB
	Elevation	0.01223 m	−12.68 dB	0.01221 m	−13.33 dB

According to the profiles in Fig. 5, the azimuth and elevation focusing quality of near and far targets are degraded, which is consistent with theoretical analysis and calculation results in Fig. 6. And the focusing quality of the simulation are listed in Table 3. It can be seen that the IRW and PSLR of the imaging result with residual phase compensation are improved comparing with the result without the compensation.

According to the analysis of the numerical simulation results, it can be concluded that the scene illuminated by 3D bistatic imaging geometry can be well reconstructed through the 3D bistatic Omega-K algorithm deduced in this paper. And Subsection 4.2 provides further verification through experiment based on near range imaging system.

4.2. Experiments

This subsection verifies the correctness and effectiveness of the imaging geometry and imaging algorithm of this paper via near range imaging experiment. Most of the experimental parameters are the same as simulation parameters, and the experiment system and illuminated scene are shown in Fig. 7.

As shown in Fig. 7, (a) shows the experimental system; (b) shows the transmitting and receiving antennas, interval of which is 0.5 m; and the illuminated scene is shown in (c). The main targets in the scene include steel square, scissor and solid metal balls, which are fixed on a

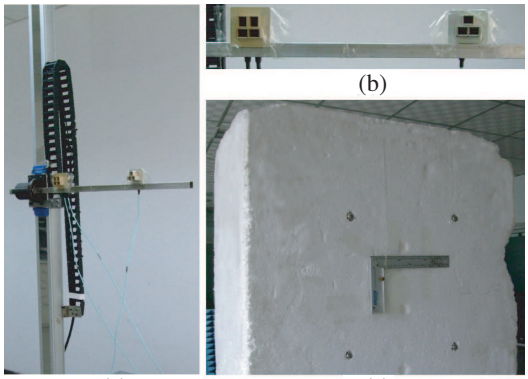

Figure 7. Experiment system and illuminated scene. (a) shows the experimental system; and (c) shows the transmitting and receiving antennas; (b) is the illuminated scene.

rectangular foam. The detailed description of the scene is as follows.

The range from scene center to scanning plane is 1.5 m. And the main targets are fixed on the front and back of the foam. In detail, the front of the foam is 1.2 m away from the scanning plane, on which several targets are fixed, including a steel square fixed with cotton thread and transparent tape, four solid metal balls of 2 cm diameter which form a shape of square with 0.4 m side length. And targets on the back of the foam, which is 1.8 m away from the scanning plane, include a scissor fixed with cotton thread and transparent tape, four solid metal balls of 2 cm diameter with the same distribution as the front ones. Besides, the scanning lengths of azimuth and elevation in the experiment are 1.3 m, and the calculating procedures of azimuth and elevation resolutions are changed into Table 4.

In order to analyze the effect of residual phase compensation, both of the images based on algorithms without and with residual phase compensation are reconstructed, and the results are shown in Fig. 8, in which the red one is the image without the compensation and the black one is the image with the compensation. It can be seen from Fig. 8 that there are certain azimuth and elevation position offset between the red and black image.

Then, the azimuth and elevation focus quality are analyzed by means of maximum projection method [1]. In detail, the 3D images in Fig. 8 are projected to azimuth — elevation plane at range of 1.2 m and 1.8 m, and the projected results are shown in Fig. 9.

In Figs. 9(a) and (b) are optical photos of the front and back of

the foam. It can be seen that main targets on the front includes a steel square and four solid metal balls marked with A, B, C and D, and main targets on the back includes a scissor and four solid metal balls marked with E, F, G and H. And (c) and (d) show the projections based on reconstructed image without compensation, in which the azimuth and elevation focus quality are degraded. Finally, (e) and (f) show the projections based on reconstructed image with compensation. In these two subfigures, not only the major targets of steel square, scissors, metal balls but also the accessories including the hole (I), screw (II) in the steel square and the plastic handle of the scissor are exactly focused. Besides, the auxiliary objects including cotton thread (III) and transparent tape (IV) are also well reconstructed. In order to display the results more clearly, the enlarged major targets projections of the 3D imaging result with residual phase compensation are shown in Fig. 10.

The experiment and the imaging results of this subsection further validate the feasibility and correctness of the proposed 3D bistatic imaging geometry and corresponding 3D bistatic Omega-K algorithm.

Table 4. Theoretical resolutions of targets located at the range of 1.2 m and 1.8 m.

	$\mathbf{Ł}'_{x,z}$	$\phi_x\mathbf{R}$	**Azimuth**	$\phi_z\mathbf{R}$	**Elevation**
Near (1.2 m)	1.3 m	0.6282 m	0.0084 m	0.7853 m	0.0067 m
Far (1.8 m)	1.3 m	0.9423 m	0.0084 m	1.1779 m	0.0067 m

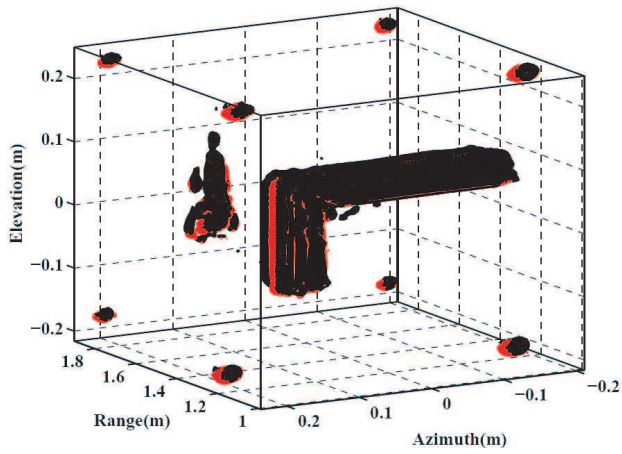

Figure 8. 3D imaging result of the experiment scenario.

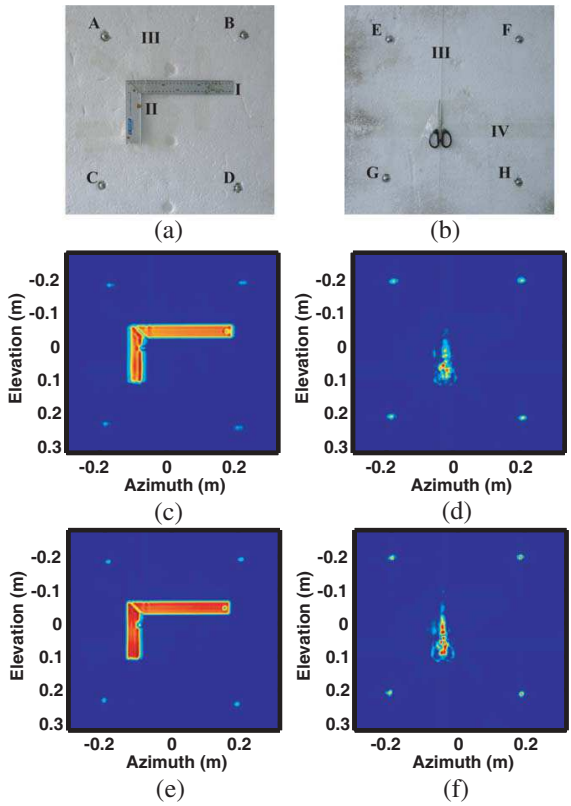

Figure 9. Projections of imaging results without and with residual phase compensation. (a) and (b) are optical photos of the front and back of the foam; (c) and (d) show the results without the compensation and (e) and (f) show the results with the compensation.

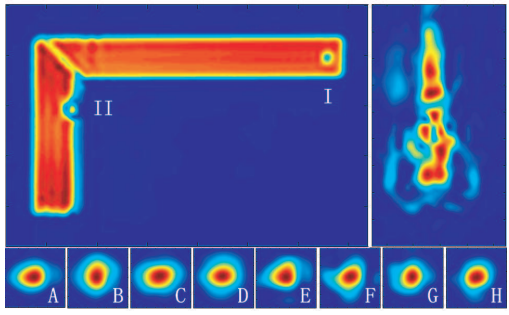

Figure 10. Enlarged projections of major targets which derived from the 3D imaging with compensation.

5. CONCLUSION

This paper proposes near range 3D bistatic imaging geometry and establishes corresponding echo model. Then, the 3D bistatic imaging algorithm based on implicit spectral decomposition are deduced and the impacts of residual phase, including position displacement, range, azimuth and elevation defocusing, are studied. Finally, the paper validates the feasibility and correctness of the 3D bistatic imaging geometry and corresponding algorithm by means of numerical simulations and experiments based on near range imaging system. The imaging results of simulations and experiments demonstrate that 3D image of illuminated scene can be well reconstructed via the 3D bistatic imaging algorithm deduced in this paper, and the method of residual phase compensation in the algorithm can improve focusing quality of the 3D image.

ACKNOWLEDGMENT

The authors would like to thank the support of the National Science Fund for Distinguished Young Scholars under Grant 60725103, the National Natural Science Foundation for Young Scientists of China under Grant No. 61002038, and the National Natural Science Foundation of China under Grant 60890070.

APPENDIX A. DESCRIPTION OF THE VARIABLES RELATED TO RESIDUAL PHASE

Table A1. Description of the variables related to residual phase.

Variable	Description
$\Phi_{res}(K_x, K_y, K_z; y)$	Total residual phase
Φ_{const}	Const phase term
$x_m(y), z_m(y)$	Linear phase terms, resulting in position displacements.
$\Phi_{err}^{rg}(K_x; y)$	Range phase error
$\Phi_{err}^{az}(K_x; y)$	Azimuth phase error, resulting in azimuth defocusing
$\Phi_{err}^{el}(K_z; y)$	Elevation phase error, resulting in Elevation defocusing
$\Phi_{err}^{ae}(K_x; K_z; y)$	Cross phase error

REFERENCES

1. Tan, W. X., W. Hong, Y. P. Wang, and Y. R. Wu, "A novel spherical-wave three-dimensional imaging algorithm for microwave cylindrical scanning geometries," *Progress In Electromagnetics Research*, Vol. 111, 43–70, 2011.
2. Fortuny, J., "Efficient algorithms for three-dimensional near-field synthetic aperture radar imaging," Ph.D. Thesis, University of Karslruhe, 2001.
3. Solimene, R., A. Brancaccio, R. D. Napoli, and R. Pierri, "3D sliced tomographic inverse scattering experimental results," *Progress In Electromagnetics Research*, Vol. 105, 1–13, 2010.
4. Gemio, J., J. Parron, and J. Soler, "Human body effects on implantable antennas for ISM bands applications: Models comparison and propagation losses study," *Progress In Electromagnetics Research*, Vol. 110, 437–452, 2010.
5. Sheen, D. M., D. L. McMakin, and T. E. Hall, "Near-field three-dimensional radar imaging techniques and applications," *Applied Optics*, Vol. 49, No. 19, 83–93, 2010.
6. Crocco, L., F. Soldovieri, T. Millington, and N. J. Cassidy, "Bistatic tomographic GPR imaging for incipient pipeline leakage evaluation," *Progress In Electromagnetics Research*, Vol. 101, 307–321, 2010.
7. Qiu, X. L., "Study on algorithms for bistatic SAR precise imaging," Ph.D. Thesis, Institute of Electronics, Chinese Academy of Sciences, 2009 (in Chinese).
8. Li, X. F., Y. J. Xie, and R. Yang, "Bistatic RCS prediction for complex targets using modified current marching technique," *Progress In Electromagnetics Research*, Vol. 93, 13–28, 2009.
9. Yan, H. H., Y. F. Wang, and H. F. Yu, "An imaging method of distributed small satellites bistatic SAR based on range distance compensation," *J. Electron. Inf. Technol.*, Vol. 27, No. 5, 771–774, 2005.
10. Qiu, X. L., D. H. Hu, and C. B. Ding, "Focusing bistatic images use RDA based on hyperbolic approximating," *CIE*, 1323–1326, Shanghai, China, 2006.
11. Walterscheid, I., A. R. Brenner, and J. H. G. Ender, "Geometry and system aspects for a bistatic airborne SAR-experiment," *EUSAR*, 567–570, Ulm, Germany, 2004.
12. Qiu, X. L., D. H. Hu, and C. B. Ding, "An Omega-K algorithm with phase error compensation for bistatic SAR of a translational invariant case," *IEEE Transactions on Geoscience and Remote*

Sensing, Vol. 46, 2224–2232, 2008.

13. Giroux, V., H. Cantalloube, and F. Daout, "An Omega-K algorithm for SAR bistatic systems," *IGRASS 2005*, 1060–1063, Seoul, Korea, 2005.
14. Sun, J. P., S. Y. Mao, G. H. Wang, and W. Hong, "Polar format algorithm for spotlight bistatic SAR with arbitrary geometry configuration," *Progress In Electromagnetics Research*, Vol. 103, 323–338, 2010.
15. Tan, W. X., "Study on theory and algorithms for three-dimensional synthetic aperture radar imaging," Ph.D. Thesis, Institute of Electronics, Chinese Academy of Sciences, 2009 (in Chinese).
16. Lopez-Sanchez, J. M. and J. Fortuny-Guasch, "3-D Radar imaging using range migration techniques," *IEEE Transactions on antennas and Propagation*, Vol. 48, 728–737, 2000.
17. Leou, J. L. and H. J. Li, "Evaluation of bistatic far-field quantities from near-field measurements," *Progress In Electromagnetics Research*, Vol. 25, 167–188, 2000.
18. Sun, J. P., S. Y. Mao, G. H. Wangm, and W. Hong, "Extended exact transfer function algorithm for bistatic SAR of translational invariant case," *Progress In Electromagnetics Research*, Vol. 99, 89–108, 2009.